

Charge density wave and superconducting phase in monolayer InSe

Mohammad Alidoosti,¹ Davoud Nasr Esfahani,^{2,3} and Reza Asgari^{1,4,5,*}

¹*School of Nano Science, Institute for Research in Fundamental Sciences (IPM), Tehran 19395-5531, Iran*

²*Pasargas Institute for Advanced Innovative Solutions(PIAIS), Tehran, Iran*

³*Department of Converging Technologies, Khatam University, Tehran, Iran*

⁴*School of Physics, Institute for Research in Fundamental Sciences (IPM), Tehran 19395-5531, Iran*

⁵*ARC Centre of Excellence in Future Low-Energy Electronics Technologies, UNSW Node, Sydney 2052, Australia*

(Dated: July 3, 2020)

In this paper, the completed investigation of a possible superconducting phase in monolayer indium selenide is determined using first-principle calculations for both the hole and electron doping systems. The hole-doped dependence of the Fermi surface is exclusively fundamental for the monolayer InSe. It leads to the extensive modification of the Fermi surface from six separated pockets to two pockets by increasing the hole densities. For quite low hole-doped of the system, below the Lifshitz transition point, a strong electron-phonon coupling $\lambda \sim 7.6$ is obtained; uniquely determining a superconductive critical temperature of $T_c = 65$ K. However, for some hole doping above the Lifshitz transition point, the combination of the temperature dependence of the bare susceptibility and the strong electron-phonon interaction gives rise to a charge density wave that emerged at a temperature far above T_c . Having included non-adiabatic effects, we could carefully analyze conditions for which either a superconductive or charge density wave phase occurs in the system. In notable addition, monolayer InSe becomes dynamically stable by including non-adiabatic effects for different carrier concentrations at room temperature.

I. INTRODUCTION

Motivated by the discovery of graphene [1], a two-dimensional (2D) advanced material with spectacular properties, researchers have greatly discovered 2D layered materials; namely, hexagonal boron nitride [2], transition metal dichalcogenide (like MoS₂ and WS₂) [3], magnetic 2D crystalline like monolayer chromium triiodide (CrI₃) [4] and other elemental 2D semiconductors like black phosphorus [5] and silicene [6], ranging from insulators, semiconductors, metals, magnetics and superconductors.

In addition, group III-VI semiconductors (M₂X₂, M = Ga and In and X = S, Se and Te) with sombrero-shaped valence band edges have shown marvelous electrical and optical properties [7, 8]. The bulk indium selenide (InSe), III-monochalcogenide semiconductor, has β , ε and γ structural phases depending on stacking characteristics [9–11]. Among these phases, ε has an indirect bandgap about 1.4 eV [10], while, β and γ phases have a direct bandgap close to 1.28 [12] and 1.29 eV [13], respectively. Electron-phonon coupling (EPC) and superconductive properties of an electron-doped monolayer InSe were studied [14] and a superconductive transition temperature about 3.41 K was reported. Moreover, it has been shown that hole states in monolayer InSe are strongly renormalized by the coupling with acoustic phonons leading to the formation of satellite quasiparticle states near the Fermi energy [15]. Not long ago, monolayer InSe has been fabricated from its bulk counterpart by mechanical exfoliation [16–18]. High carrier mobility

about 10^3 cm²/Vs, which is greater than that of MoS₂ [19], has been reported at room temperature [20]; suggesting that this 2D material is promising for ultra-thin digital electronics applications. Furthermore, InSe is a promising material for making use of FETs [21].

The presence of the sombrero-shaped valence band in the electronic band structure of monolayer InSe gives rise to a larger density of states (DOS), which is similar to that of one-dimensional material, specifies a Van Hove singularity at the valence band maximum (VBM) which could primarily lead to a magnetic transition and superconducting phases as well [22–26]. Stimulated by the remarkable discovery of gate-induced superconductivity in graphene (upon lithium adsorption) [27–30], a new field for investigating superconducting features on the other 2D materials typically emerges. In advance, lithium adsorbed graphene was properly utilized for 2D superconductivity. Undoubtedly owing to a small DOS at the Fermi level and the σ_h symmetry which gives rise to a weakened electron coupling with the flexural modes, graphene illustrates a small electron-phonon coupling constant, λ . However, these shortcomings could be lifted by typically making use of lithium adsorption [29, 30].

Even though monolayer InSe naturally has σ_h symmetry, electrons in monolayer InSe could couple to the flexural phonons owing to the presence of the atomic layers away from the symmetry plane. Notably, this coupling alongside with a larger DOS near the VBM potentially leads to a large EPC parameter. On the other hand, the active presence of a significant DOS as well as λ makes the system susceptible to a charge density wave (CDW) instability, which represents a static modulation of the itinerant electrons and usually accompanied by a periodic distortion of the lattice. The CDW formation may naturally arise from a possible combination of the large

*Electronic address: asgari@ipm.ir

nesting and/or electron-phonon interaction at a specific phonon wave vector (\mathbf{q}_{CDW}). Therefore, the formation of the CDW must be carefully examined for systems with a strong EPC, though a superconducting state is possible.

The standard method of properly investigating the CDW formation is first to calculate the phonon dispersion of the system within density functional theory (DFT) calculations, i.e. considering either a small displacement or density functional perturbation theory (DFPT) method at specific temperatures [31]. It is worth mentioning that the static electron-phonon interactions induced phonon self-energy are carefully considered in the phonon dispersion of both mentioned approaches [32]. However, it has become evident that dynamical phonons undoubtedly play a significant role and non-adiabatic/dynamic effects could give rise to a significantly renormalized phonon dispersion for doped semiconducting materials [33–35] including InSe.

Here, we adequately investigate a viable superconducting and CDW phases of monolayer InSe based on DFT and necessary DFPT calculations. We correctly calculate the renormalized phonon dispersion owing to the electron-phonon coupling in both the adiabatic and non-adiabatic regimes for different temperatures and doping levels. We further investigate the competition between CDW formation and the superconductive phase for the different hole and electron doping levels. We eagerly discuss the most important phonon wave vectors leading to the remarkable electron-phonon coupling strength which well expresses the significance of both bare susceptibility and nesting function below and above the Lifshitz transition point. By including non-adiabatic effects, we carefully analyze conditions for which either a superconductive or CDW phase could typically emerge in the system. Our desired results show that in some hole-doped cases, the CDW instability prevents access to the quite high-temperature superconductivity, whereas, for some other doped levels, the achievement of such superconducting temperatures is possible. In the electron-doped cases, the CDW instability is significantly suppressed, and therefore, the superconducting phase is possible.

The paper is organized as follows. We commence with a description of our theoretical formalism in Sec. II, followed by the details of the DFT and DFPT calculations. Numerical results for the band structures, phonon dispersions, DOS, superconducting critical temperature, and CDW in adiabatic and non-adiabatic approximations are reported in Sec. III. We summarize our main findings in Sec. IV.

II. THEORY AND COMPUTATIONAL DETAILS

The self-consistent DFT calculations are carefully performed with LDA-Norm-conserving pseudopotential as implemented in Quantum Espresso package [36]. The phonon dispersion and self-consistent deformed potentials are calculated based on DFPT method [31, 32, 37].

The Kohn-sham wave functions and Fourier expansion of the charge density are truncated at 90 and 360 Ry, respectively. To eliminate spurious interaction between adjacent layers, a vacuum space of 25 Å along the z -direction is adopted. For the electronic and phononic calculations, a $24 \times 24 \times 1$ \mathbf{k} -mesh and $12 \times 12 \times 1$ \mathbf{q} -mesh, are used and a finer \mathbf{k} -mesh $240 \times 240 \times 1$ and \mathbf{q} -mesh $120 \times 120 \times 1$, respectively, are applied to calculate the Wannier interpolation of the electronic and phonon dispersions as implemented in EPW code [38–41]. The Dirac delta functions are approximated by applying the Gaussian smearing $\sigma_{el} = 5$ meV and $\sigma_{ph} = 0.2$ meV. The convergence of results is carefully performed as a function of the \mathbf{k} - and \mathbf{q} -mesh and Gaussian smearing. Moreover, to adequately describe the temperature dependence of the electronic structure, the Fermi-Dirac smearing about 0.01 Ry is used [42].

Since the static part of the phonon self-energy is typically included in the phonon dispersion, one may uniquely define a dressed phonon frequency as [43],

$$\omega_{\mathbf{q},\nu}^2 = \Omega_{\mathbf{q},\nu}^2 + 2\omega_{\mathbf{q},\nu}\Pi_{\mathbf{q},\nu}, \quad (1)$$

where $\Omega_{\mathbf{q},\nu}$ is the bare phonon frequency and $\Pi_{\mathbf{q},\nu} = \frac{2}{N_{\mathbf{k}}} \sum_{\mathbf{k},m,n} |g_{n\mathbf{k},m\mathbf{k}+\mathbf{q}}^{\nu}|^2 \frac{f(\epsilon_{n\mathbf{k}}) - f(\epsilon_{m\mathbf{k}+\mathbf{q}})}{\epsilon_{n\mathbf{k}} - \epsilon_{m\mathbf{k}+\mathbf{q}}}$ is the static part of the first-order self-energy of phonon modes, m and n refer to the electronic band indexes, $N_{\mathbf{k}}$ is the considerable number of \mathbf{k} points, $g_{mn,\nu}(\mathbf{k}, \mathbf{q})$ is the electron-phonon interaction matrix elements and $f(\epsilon)$ represents the Fermi-Dirac distribution function.

It is reasonable to assume \mathbf{k} independent electron-phonon interactions in which $g_{n\mathbf{k},m\mathbf{k}+\mathbf{q}}^{\nu} = g_{\mathbf{q}n,m}^{\nu}$. Therefore, Eq. (1) can be written as follows;

$$\omega_{\mathbf{q},\nu}^2 = \Omega_{\mathbf{q},\nu}^2 + 2\omega_{\mathbf{q},\nu}|g_{\mathbf{q}n,m}^{\nu}|^2\chi_0(\mathbf{q}). \quad (2)$$

with $\chi_0(\mathbf{q}) = \frac{2}{N_{\mathbf{k}}} \sum_{\mathbf{k},m,n} \frac{f(\epsilon_{n\mathbf{k}}) - f(\epsilon_{m\mathbf{k}+\mathbf{q}})}{\epsilon_{n\mathbf{k}} - \epsilon_{m\mathbf{k}+\mathbf{q}}}$ is the bare charge susceptibility. The phonon softening typically emerges at some branches of the phonon spectrum, known as Kohn anomaly [44] which originates from any sizable variation of χ_0 as a function of \mathbf{q} and/or the electronic temperature. Consequently, it is a common practice to scientifically verify χ_0 as a necessary signature of the phonon softening and thus the formation of the CDW. The CDW instability can be well-appeared in the form of an imaginary phonon band when temperature lies below T_{CDW} (the temperature where softened modes touch the zero frequency at \mathbf{q}_{CDW}).

To estimate superconducting temperature in systems with strong EPC, we utilize Migdal-Eliashberg formalism [45, 46] in the form of modified Allen-Dynes parametrization [47]:

$$T_c = \frac{f_1 f_2 \omega_{\log}}{1.2} \exp\left(-\frac{1.04(1+\lambda)}{\lambda - \mu_c^*(1+0.62\lambda)}\right), \quad (3)$$

with $\lambda = 2 \int_0^{\infty} \omega^{-1} \alpha^2 \mathbf{F}(\omega) d\omega$, $\omega_{\log} = \exp\left[\frac{2}{\lambda} \int_0^{\omega_{\max}} d\omega \frac{\alpha^2 \mathbf{F}(\omega)}{\omega} \log \omega\right]$, μ_c^* is Morel-Anderson

coulomb potential, and we use $\mu_c^* = 0.1$, f_1 and f_2 represent strong-coupling and shape corrections, respectively (for detail definitions of f_1 and f_2 see Ref. [47]). The Eliashberg function is defined as,

$$\alpha^2 \mathbf{F}(\omega) = \frac{1}{N(\varepsilon_F) N_{\mathbf{k}} N_{\mathbf{q}}} \sum_{\substack{\mathbf{q}, \mathbf{k} \\ \nu, m, n}} |g_{mn, \nu}(\mathbf{k}, \mathbf{q})|^2 \times \quad (4)$$

$$\delta(\varepsilon_{n\mathbf{k}} - \varepsilon_F) \delta(\varepsilon_{m\mathbf{k}+\mathbf{q}} - \varepsilon_F) \delta(\omega - \omega_{\mathbf{q}\nu}),$$

where $N(\varepsilon_F)$ is the electronic density of states at the Fermi level. The imaginary part of the phonon self-energy $\gamma_{\mathbf{q}\nu}$ reads as follows;

$$\gamma_{\mathbf{q}\nu} = \frac{2\pi\omega_{\mathbf{q}\nu}}{N_{\mathbf{k}}} \sum_{mn, \mathbf{k}} |g_{mn, \nu}(\mathbf{k}, \mathbf{q})|^2 \delta(\varepsilon_{n\mathbf{k}} - \varepsilon_F) \delta(\varepsilon_{m\mathbf{k}+\mathbf{q}} - \varepsilon_F), \quad (5)$$

To carefully analyze the different contributions of the λ and $\alpha^2 \mathbf{F}$, the projected quantities are defined as follows. Two principal directions are typically considered; in-plane and out-of-plane distortions. The $\mathbf{F}(\omega)$ along the specific direction κ is written as

$$\mathbf{F}^{\kappa}(\omega) = \sum_{s, \nu} \int \frac{d\mathbf{q}}{(2\pi)^2} \mathbf{P}_{\mathbf{q}\nu}^{\kappa, s} \delta(\omega - \omega_{\mathbf{q}\nu}), \quad (6)$$

for the atom type s in the unit cell (including In_2 or Se_2) where $\kappa = \overline{xy}$ (labeled by in-plane), \overline{z} (labeled by out-of-plane) and

$$\mathbf{P}_{\mathbf{q}, \nu}^{\overline{xy}, s} = \sum_{\kappa=x, y} \mathbf{e}_{\mathbf{q}, \nu}^{* \kappa, s} \mathbf{e}_{\mathbf{q}, \nu}^{\kappa, s}, \quad \mathbf{P}_{\mathbf{q}, \nu}^{\overline{z}, s} = \mathbf{e}_{\mathbf{q}, \nu}^{* z, s} \mathbf{e}_{\mathbf{q}, \nu}^{z, s}, \quad (7)$$

where vector $\mathbf{e}_{\mathbf{q}\nu}$ is the eigenvector of the dynamical matrix. The $\alpha^2 \mathbf{F}$ can also be projected into Cartesian coordinates by making use of the phonon displacements associated with various atom types in different directions.

$$\alpha^2 \mathbf{F}_{s, s'}^{\kappa, \kappa'}(\omega) = \frac{1}{N_{\mathbf{k}} N_{\mathbf{q}} N(\varepsilon_F)} \sum_{m, n, \nu, \mathbf{k}, \mathbf{q}} g_{n\mathbf{k}, m\mathbf{k}+\mathbf{q}, \nu}^{* \kappa, s} g_{n\mathbf{k}, m\mathbf{k}+\mathbf{q}, \nu}^{\kappa', s'} \times \delta(\varepsilon_{n\mathbf{k}} - \varepsilon_F) \delta(\varepsilon_{m\mathbf{k}+\mathbf{q}} - \varepsilon_F) \delta(\omega - \omega_{\mathbf{q}\nu}), \quad (8)$$

where κ, κ' refer to the in-plane and out-of-plane deformations, respectively with $g_{n\mathbf{k}, m\mathbf{k}+\mathbf{q}, \nu}^{\overline{xy}, s} = \sum_{\kappa=x, y} (\frac{\hbar}{2\omega_{\mathbf{q}\nu}})^{1/2} d_{n\mathbf{k}, m\mathbf{k}+\mathbf{q}}^{\kappa, s} u_{\mathbf{q}\nu}^{\kappa, s}$ and $g_{n\mathbf{k}, m\mathbf{k}+\mathbf{q}, \nu}^{\overline{z}, s} = (\frac{\hbar}{2\omega_{\mathbf{q}\nu}})^{1/2} d_{n\mathbf{k}, m\mathbf{k}+\mathbf{q}}^{z, s} u_{\mathbf{q}\nu}^{z, s}$ and $u_{\mathbf{q}}^{\kappa, s} = \frac{\mathbf{e}_{\mathbf{q}}^{\kappa, s}}{\sqrt{m_s}}$ is displacement pattern [48], so that $\alpha^2 \mathbf{F}_{s, s'}^{\kappa, \kappa'}$ satisfies the following relation

$$\alpha^2 \mathbf{F}(\omega) = \sum_{k, k', s, s'} \alpha^2 \mathbf{F}_{s, s'}^{\kappa, \kappa'}(\omega). \quad (9)$$

In particular, we define $\alpha^2 \mathbf{F}_{\overline{z}, \overline{xy}}(\omega) = 2 \sum_{s, s'} \sum_{k' = x, y} \Re[\alpha^2 \mathbf{F}_{s, s'}^{z, \kappa'}(\omega)]$, $\alpha^2 \mathbf{F}_{\overline{xy}, \overline{xy}}(\omega) =$

$\sum_{s, s'} \sum_{k, k' = x, y} \alpha^2 \mathbf{F}_{s, s'}^{\kappa, \kappa'}(\omega)$ and $\alpha^2 \mathbf{F}_{\overline{z}, \overline{z}}(\omega) = \sum_{s, s'} \alpha^2 \mathbf{F}_{s, s'}^{z, z}(\omega)$. Projected λ can be obtained by projected $\alpha^2 \mathbf{F}$ as following

$$\lambda_{s, s'}^{\kappa, \kappa'} = 2 \int d\omega \frac{\alpha^2 \mathbf{F}_{s, s'}^{\kappa, \kappa'}(\omega)}{\omega}. \quad (10)$$

III. NUMERICAL RESULTS AND DISCUSSIONS

Two distinct types of structural phases (α and β) have been properly reported for pristine monolayer InSe in Ref. [8] which α phase has mirror symmetry, while β has inversion symmetry. Moreover, both of them are dynamically stable, but, the former possesses cohesive energy slightly lower than the latter. We efficiently perform our DFT calculations on α phase by incorporating a hexagonal structure with D_{3h} symmetry. The relaxed geometry calculations of pristine monolayer InSe show that the optimized hexagonal unit cell naturally has the lattice constant $a = 3.90 \text{ \AA}$ and two sublayers are separated by distance $d_{\text{In-In}} = 2.66 \text{ \AA}$ and $d_{\text{Se-Se}} = 5.15 \text{ \AA}$. These parameters are in good agreement with previous studies [8, 14, 25].

A. Investigation of superconductive properties of monolayer InSe

In this work, both the electron- and hole-doped cases are carefully studied within the jellium model for monolayer InSe. A compensate positive or negative background charge is included to guarantee the charge neutrality.

There are different experimental techniques like electrolytic gate [49] to precisely control the rate of the electron and hole densities. Here, we consider electron doping levels -0.1 and -0.2 electron per formula unit (e/f.u.) precisely corresponding to the electron densities, 7.44×10^{13} and $1.46 \times 10^{14} \text{ cm}^{-2}$ respectively. Similarly, $+0.01, +0.04$ (low doping regime), $+0.1, +0.2, +0.3$ and $+0.4$ e/f.u. (high doping regime) for hole-doped cases corresponding to $7.58 \times 10^{12}, 3.0 \times 10^{13}, 7.58 \times 10^{13}, 1.51 \times 10^{14}, 2.26 \times 10^{14}$ and $3.0 \times 10^{14} \text{ cm}^{-2}$ charge densities are considered. For the sake of simplicity, we promptly drop e/f.u. units corresponding to different doping levels, \pm refers to the hole or electron doping, respectively.

The Fermi surfaces of the system are described in Fig. 1 for different doping levels. Fig. 1(a) displays the topology of the Fermi surface for -0.1 doping consisting precisely of two types of electronic pockets located at the Γ and M points. In the case of the deeper electronic doping level -0.2 , the specific form of the Fermi surface is similar to the previous doping level. The Fermi surface of $+0.04$

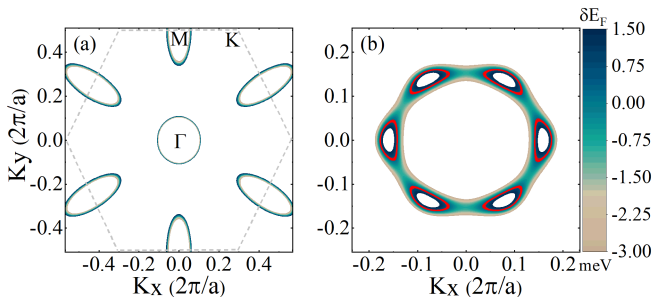


FIG. 1: (Color online) The Fermi surface contour of the monolayer InSe based on the jellium model. (a) The Fermi surface for doping -0.1 . (b) The Fermi surfaces corresponding to different shifts of the E_F from the E_F related to the doping level $+0.04$ (represented by red lines). The color bar shows the shift of the Fermi energy. The gray dashed lines are applied to illustrate the first Brillouin zone boundaries.

doping system consists of six separated pockets located around a point between the Γ and \mathbf{K} as shown in Fig. 1 marked by red color.

In the hole-doped case (see Fig. 1(b)) and upon more significantly decreasing the Fermi energy E_F , a Lifshitz transition [8] occurs. Therefore, the topology of the Fermi surface with six pockets, located between the Γ and \mathbf{K} , changes to two coaxial pockets around the Γ point. This fundamental change of the principal character of the Fermi surface results in a tangible variation of superconductive properties of the hole-doped system which we adequately address in the following.

To begin with, we carefully look at the Eliashberg function in terms of various doping levels. Figs. 2(a) and (b) depict the $\alpha^2\mathbf{F}(\omega)$ and projected phonon DOS for doping level -0.1 . The projected Eliashberg function along the in-plane and out-of-plane deformations show a mighty peak at around 27 meV related to a scattering process which originates primarily from $\alpha^2\mathbf{F}_{\bar{z},\bar{xy}} + \alpha^2\mathbf{F}_{\bar{z},\bar{z}}$ resulting of the out-of-plane vibration of In atoms and in-plane vibration of Se atoms. This is equally consistent with the projected $\mathbf{F}(\omega)$ in Fig. 2(b), where there is significant density of phonons with In_z and Se_{xy} deformations. Looking at more reduced energies there is a two-peak structure between 21–24 meV, where the larger one forms from $\alpha^2\mathbf{F}_{\bar{z},\bar{xy}} + \alpha^2\mathbf{F}_{\bar{z},\bar{z}}$, while the more lesser peak comes from $\alpha^2\mathbf{F}_{\bar{z},\bar{xy}} + \alpha^2\mathbf{F}_{\bar{xy},\bar{xy}}$. On the other hand, peaks at more reduced energies originate from $\alpha^2\mathbf{F}_{\bar{xy},\bar{xy}}$.

The $\alpha^2\mathbf{F}(\omega)$ and $\mathbf{F}(\omega)$ are shown in Figs. 2(c) and (d) for low hole doping level $+0.01$. There is a peak around 28 meV, which comes principally from single optical phonon mode with the out-of-plane In and in-plane Se vibrations. In this case, the deformation of the $\alpha^2\mathbf{F}_{\bar{z},\bar{z}}$ is considerably larger than $\alpha^2\mathbf{F}_{\bar{z},\bar{xy}}$. Moreover, the small peak at around 26 meV has a major $\alpha^2\mathbf{F}_{\bar{xy},\bar{xy}}$ and a minor $\alpha^2\mathbf{F}_{\bar{z},\bar{z}}$ character with a destructive contribution from $\alpha^2\mathbf{F}_{\bar{z},\bar{xy}}$, while the strong peak at around 8 meV has a major $\alpha^2\mathbf{F}_{\bar{z},\bar{xy}}$ character with relatively equal contributions from the other two deformations.

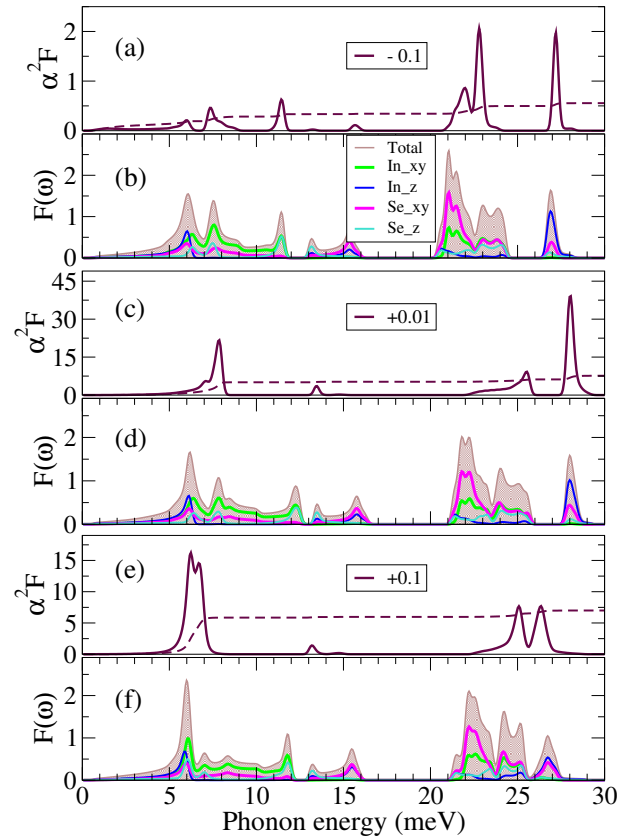


FIG. 2: (Color online) The $\alpha^2\mathbf{F}$ and projected phonon DOS within the jellium model. (a), (c) and (e) Total $\alpha^2\mathbf{F}$ and cumulative EPC, $\lambda(\omega)$, for specific doping levels -0.1 , $+0.01$ and $+0.1$. The dashed lines are used for $\lambda(\omega)$. (b), (d) and (f) refer to the projected phonon DOS, $\mathbf{F}(\omega)$, respectively, for In and Se atoms along the in-plane and out-of-plane directions for corresponding doping levels.

As a notable example of high hole-doped regime, the $\alpha^2\mathbf{F}(\omega)$ and projected $\mathbf{F}(\omega)$ for $+0.1$ are shown in Figs. 2(e) and (f), respectively. Despite the low hole-doped and electron-doped cases, the prominent peak around 28 meV is absent. In general, the spectrum of $+0.1$ hole-doped is slightly shrunk in comparison with $+0.01$ one. Moreover, the gapped two peaks structure in the high energy part of the $\alpha^2\mathbf{F}(\omega)$ for $+0.01$ is replaced with a gapless one at the energy about 25–27 meV. The outstanding contribution of this high energy part arises mainly from the $\alpha^2\mathbf{F}_{\bar{z},\bar{z}}$ and $\alpha^2\mathbf{F}_{\bar{xy},\bar{xy}}$ deformations, however, the $\alpha^2\mathbf{F}_{\bar{z},\bar{xy}}$ has a completely destructive contribution. The low-energy peak between 5–7 meV has almost the identical character as the low-energy peak of the $+0.01$ doping level, albeit with a lesser height.

Therefore, passing through Lifshitz transition point results in a tangible modulation of the optical phonons which could significantly affect their superconductive properties. Notice that, the Eliashberg function for the specific case of $+0.01$ behaves properly something between electron doping and high hole-doped cases.

As a result, we can correctly state that in hole doping the acoustic branches carry out a substantial role in the formation of the λ_{tot} . Unlike hole-doped cases, there is a more uniform distribution of each branch contributing in the formation of the λ_{tot} for the electron doping, as inferred from $\lambda(\omega)$ in Figs. 2(a), (c) and (e).

Tabulated amounts of λ_{tot} with respect to various doped levels in Table. I reveal that upon increasing in the hole/electron doping levels leads to a descending/constant behavior of the λ_{tot} , respectively. Obviously, while the amount of the λ is almost the same for the first three hole-doped cases, the T_c for +0.01 is 30 percent larger than that of +0.1; coming from a larger value of ω_{log} . The larger value of the ω_{log} corresponding to the former originates from the fact that the phonon dispersion for +0.01 doped is typically harder than +0.1. Moreover, the proportion of the high energy peak to the low-energy peak of the $\alpha^2\mathbf{F}$ for the case of +0.01 is appreciably larger than that of +0.1 (see Figs. 2(c) and (e)). Thus, the ω_{log} is enhanced for +0.01 in comparison with +0.1.

One can seemly remark that λ can take effect from $N(\varepsilon_F)$ and the average of the electron-phonon matrix elements on the Fermi surface, $\langle |g|^2 \rangle = \frac{1}{N(\varepsilon_F)} \int \alpha^2\mathbf{F}(\omega)d\omega$; according to $\lambda = 2N(\varepsilon_F)\langle |g|^2 \rangle/\omega_0$. It promptly turns out that the λ is a linear function of $N(\varepsilon_F)$ as long as $\langle |g|^2 \rangle$ and ω_0 are constant. $\lambda/\lambda_{\text{max}}$ and $N(\varepsilon_F)/N(\varepsilon_F)_{\text{max}}$ are shown in Fig. 3 for different doping levels. Upon progressively increasing the hole density, while λ decreases monotonously, the $N(\varepsilon_F)$ increases up to doping level +0.1 then decreases for larger doping levels. Accordingly, the $\langle |g|^2 \rangle$ behaves differently below and above the Lifshitz transition point. In that manner, we reasonably expect a larger $\langle |g|^2 \rangle$ for low hole doping levels, as shown in Fig. 3. Beyond doping level +0.1 a constant behavior for the $\langle |g|^2 \rangle$ can be correctly estimated for all hole-doped levels as both the $\lambda/\lambda_{\text{max}}$ and $N(\varepsilon_F)/N(\varepsilon_F)_{\text{max}}$.

In the case of electron doping, as electron density increases, a practically constant behavior of the $N(\varepsilon_F)$, λ and $\langle |g|^2 \rangle$ occur as a function of doping level. Although there exists precisely a drastic decline in the $N(\varepsilon_F)$ compared with that of hole ones, $\langle |g|^2 \rangle$ adopts those results obtained for high hole doping, and, therefore, almost a constant behavior of the $\langle |g|^2 \rangle$ is obtained as a function of the doping level.

Furthermore, Eq. (10) is properly used to carefully consider the contribution of the projected λ for different atom types and the out-of/in-plane directions in the λ_{tot} . Fig. 4 shows the projected λ while those are rescaled to the λ_{tot} for four doping levels $-0.1, +0.01, +0.1$ and $+0.4$. The desired results show, for electron doped case, the highest contribution of the λ_{tot} is attributed to the in-plane displacements. For -0.1 the corresponding in-plane/out-of-plane contributions are $\lambda_{\overline{xy},\overline{xy}} = 0.73 > \lambda_{\overline{z},\overline{z}} = 0.27 > \lambda_{\overline{z},\overline{xy}} = -0.45$.

For the hole-doped levels beyond +0.1, on the other

TABLE I: The superconducting properties of the monolayer InSe including the EPC constant, λ_{tot} , average logarithmic phonon frequency, ω_{log} , transition temperature to superconducting phase, T_c , transition temperature to CDW region, T_{CDW} , for studied hole/electron concentrations. The charge density is in units of 10^{13} cm^{-2} . We set $\mu^* = 0.1$ in all calculations.

e/f.u.	charge density	λ_{tot}	$\omega_{\text{log}}(\text{K})$	$T_c(\text{K})$	$T_{CDW}(\text{K})$
+0.01	0.758	7.62	123	65	120
+0.04	3.0	7.36	106	55	145
+0.1	7.58	6.99	90	44	420
+0.2	15.1	3.07	79	21	530
+0.3	22.6	1.44	78	9	470
+0.4	30	0.85	80	4	2
- 0.1	7.44	0.55	97	2	< 2
- 0.2	14.6	0.50	103	2	< 2

hand, the meaningful contribution arises from the out-of-plane deformations and mixed the in-plane In and out-of-plane Se constructive deformations in this case, with $\lambda_{\overline{z},\overline{z}} = 2.73 > \lambda_{\overline{z},\overline{xy}} = 2.7 > \lambda_{\overline{xy},\overline{xy}} = 1.55$. In the case of +0.01 doping, the system is some where between a high hole doping and electron doped cases. While its in-plane contributions share the same behaviour as of the electron doped one, its out-of-plane and mixed in-plane/out-of-plane contributions behave properly similar to the high doping levels, $\lambda_{\overline{z},\overline{z}} = 2.88 > \lambda_{\overline{xy},\overline{xy}} = 2.48 > \lambda_{\overline{z},\overline{xy}} = 2.26$. To be specific, the valuable contribution which comes from ($\text{In}_{\text{in}}\text{-Se}_{\text{out}}$) deformation is destructive for the electron-doped system, while it is constructive for low and high hole-doped cases. This main difference originates from the distinction between the generic forms of the topology of the Fermi surface such that this type of polarization is beneficial for hole-doped cases and it is a disadvantage of the electron-doped ones.

Furthermore, Table. I shows the critical transition temperature to the superconducting phase with the aforementioned doped conditions calculated through Eq. (3). In the case of hole doping, the highest value of $T_c = 65 \text{ K}$ is obtained. This temperature is comparable with $T_c = 88 \text{ K}$ for blue phosphorene studied in Ref. [50]. Moreover, it is much larger than reported T_c for Li-decorated monolayer graphene and antimonene with $T_c \approx 6$ [27] and 4 K [51], respectively. However, the high value of the λ needs careful examination and further insights of the formation of the CDW phase at low temperatures for the hole-doped system which we adequately address in the following section.

B. CDW formation in adiabatic approximation

Fig. 5 depicts the amplitude of the Kohn anomaly as a function of the electronic Fermi-Dirac smearing for doping level +0.1. Typically decreasing the temperature

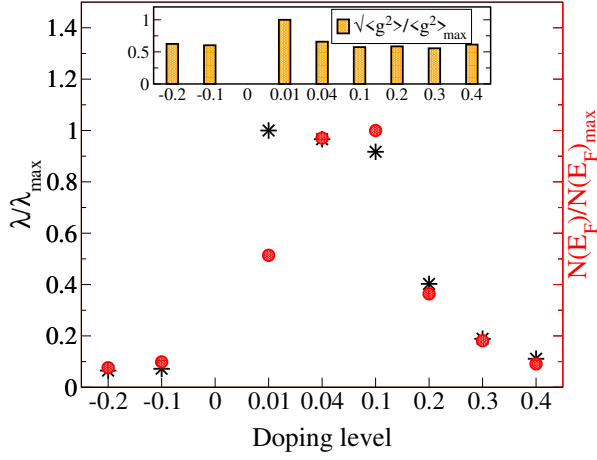


FIG. 3: (Color online) The variation of the rescaled EPC and $N(\varepsilon_F)$ with respect to different doping levels in monolayer InSe. Inset: The $\sqrt{\langle g^2 \rangle} / \langle g^2 \rangle_{max}$ as a function of the doping level. In the case of hole doping, an increment in the carrier density leads to a decreasing of both the λ/λ_{max} and $N(\varepsilon_F)/N(\varepsilon_F)_{max}$ and nearly constant value for the $\sqrt{\langle g^2 \rangle} / \langle g^2 \rangle_{max}$. While, in the case of electron doping, an increment in the carrier density leads to a constant behavior of the λ/λ_{max} , $N(\varepsilon_F)/N(\varepsilon_F)_{max}$ and $\sqrt{\langle g^2 \rangle} / \langle g^2 \rangle_{max}$.

leads to more softening of the phonon energies and finally, the system suffers from a CDW instability at smearing slightly lower than 420 K. For exploring the considerable variations of the phonon softening as a function of the Fermi-Dirac smearing, two upper temperature, 470 and 1580, in the adiabatic/static regime are depicted as well. The typical smearing 1580 K, as a starting point in the adiabatic regime, is large enough to wipe out the Kohn anomaly in linear response calculations.

In addition, this figure shows there are two \mathbf{q}_{CDW} which give rise to two different chirality. One includes a 6×6 commensurate supercell corresponding to the dip in the middle of the Γ -K direction. The secondary point of the CDW instability is related to an incommensurate distortion precisely corresponding to another dip along the Γ -M path. Our numerical calculations reveal that the dip in the middle of the Γ -K direction has lower ω^2 and we, therefore, refer to this point as \mathbf{q}_{CDW} in the reminder. Notice that for the other higher doped levels, i.e. +0.2 and +0.3 the CDW forms at the same \mathbf{q} for the +0.1 doping level. On the other hand, in the adiabatic regime, low hole doping levels +0.01 and +0.04 show instability in a \mathbf{q} different from the high doped regime. However, it does not show any instability of the system even at very low temperatures by including non-adiabatic effects. Besides, in the comparison between low doped and high doped regimes in terms of phonon softening at \mathbf{q}_{CDW} , we thus report our results at \mathbf{q}_{CDW} for doping levels +0.01 and +0.04 as well. The CDW instability indeed relies on the existence of the remarkable amounts of the λ . Hence, five cases +0.01, +0.04, +0.1, +0.2 and +0.3, with strong

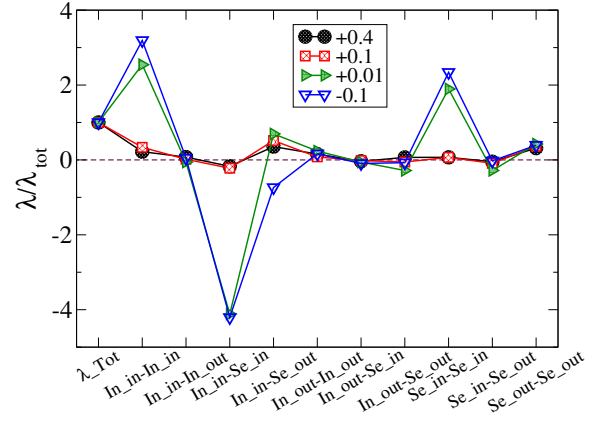


FIG. 4: (Color online) The projected λ associated with different displacements of atoms along with the in/out-of-plane directions for doping +0.4, +0.1, +0.01, and -0.1. The λ parameter is rescaled to the λ_{tot} . The dashed maroon line set to zero indicates the constructive or destructive role of the polarization. The splines connecting the points are used to guide for eyes.

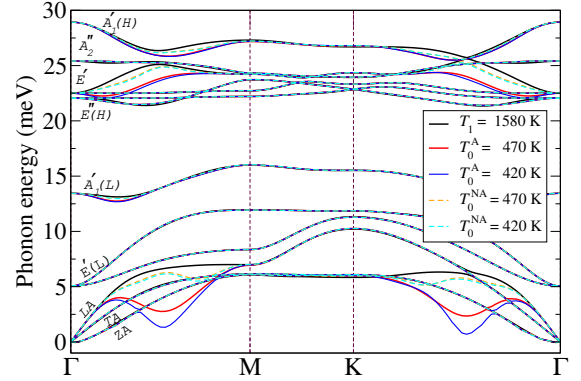


FIG. 5: (Color online) The phonon dispersion as a function of electronic temperatures for a doping +0.1 in both adiabatic (A) and non-adiabatic (NA) regimes. The lower electronic smearing, the appearance of the greater amplitude of the Kohn anomaly which finally leads to CDW instability at a temperature lower than $T_0 = 420$ K in the adiabatic regime while these anomalies can be faded out at upper temperature such as $T_0 = 470$ K. Also, fading out of the Kohn anomalies via the non-adiabatic effects compared with adiabatic one are represented for two aforementioned temperatures. The black solid lines were carried out with typical electronic broadening, $T_1 = 1580$ K, which is large enough to wipe out the Kohn anomaly in linear response self-consistent force constants.

EPC, naturally need more comprehensive considerations. To further perceive the fundamental reason for the phonon-softening, Fig. 6 shows different quantities associated with the CDW formation for various doping levels and temperatures. In particular, the average amounts of the electron-phonon interaction $\langle \mathbf{g}^2 \rangle_{\mathbf{q}\nu} = \frac{\gamma_{\mathbf{q}\nu}}{2\pi\omega_{\mathbf{q}\nu}\xi_{\mathbf{q}}}$, where the nesting function is precisely defined as $\xi_{\mathbf{q}} = N_{\mathbf{k}}^{-1} \sum_{mn,\mathbf{k}} \delta(\varepsilon_{n\mathbf{k}} - \varepsilon_F) \delta(\varepsilon_{m\mathbf{k}+\mathbf{q}} - \varepsilon_F)$, is properly used. Tilde symbol in Fig. 6 typically refers to the related cal-

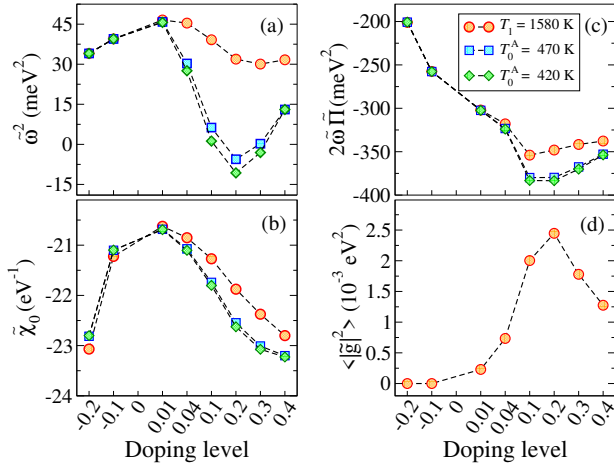


FIG. 6: (Color online) The effective factors to determine the CDW instability as a function of temperature for all doped levels. (a) The dressed phonon energies squared, (b) electronic bare susceptibility, (c) real part of the phonon self-energy, and (d) the magnitude of $\langle \tilde{g}^2 \rangle$ related to the softening branch of phonon dispersion. The splines connecting the points are guides to the eyes and the tilde symbol refers to related calculations at \mathbf{q}_{CDW} .

culations at the \mathbf{q}_{CDW} . Moreover, the depicted quantities are associated with the softened branch at \mathbf{q}_{CDW} , therefore, the branch index ν is dropped.

The effects of the phonon energy renormalization as a function of temperature within the adiabatic/static regime are shown in Fig. 6(a). These results reveal the tendency of the system to the CDW region for the three +0.1, +0.2, and +0.3 doping levels. On the contrary, the electron-doped and low hole doping levels, below the Lifshitz transition point, almost retain their constant behavior as a function of various temperatures. Fig. 6(b) shows the bare susceptibility as a function of doped levels at the \mathbf{q}_{CDW} for the aforementioned temperatures. Notice, the $\langle \tilde{g}^2 \rangle$ is the largest for doping level +0.2 (see Fig. 6(d)), in addition, the largest change of the χ_0 basically belongs to the doping level +0.2. This leads to further decline of $2\tilde{\omega}\tilde{\Pi}$ (from temperature 1580 K) for doping level +0.2 as shown in Fig. 6(c). Moreover, such a larger variation in the χ_0 for doping levels +0.1, +0.2, and +0.3 leads to a giant Kohn anomaly and finally the appearance of the instability in the monolayer InSe for smearing lower than 420, 530 and 470 K, respectively. A comparison for doping +0.4 implicitly expresses that though there is the reduction of the self-energy correction, having less temperature dependence on the χ_0 together with a smaller average of the $\langle \tilde{g}^2 \rangle$ (Fig. 6(d)) on the Fermi surface, results in less effective Kohn anomaly and therefore, the CDW is suppressed at the \mathbf{q}_{CDW} for doping level +0.4.

Further analyses associated with the polarization of the softened mode at the \mathbf{q}_{CDW} adequately explain that the instability at this point mainly involves the in-plane displacements of the In atoms and the out-of-plane displacements of the Se atoms at the same time.

The notable absence of the Kohn anomaly for electron doping is owing to the lack of a reduction of the χ_0 with respect to the different temperatures alongside with extremely small $\langle \tilde{g}^2 \rangle$ (Fig. 6(d)). In two low hole doping cases, the $\langle \tilde{g}^2 \rangle$ is smaller than that obtained for other hole-doped levels. For doping level +0.01 a specific combination of a small $\langle \tilde{g}^2 \rangle$ and the lack of typically decreasing of the χ_0 as a function of temperature results in the absence of the Kohn anomaly at \mathbf{q}_{CDW} . In doping level +0.04, although there correctly is a depletion in the χ_0 upon temperature reduction, due to a slight value of the $\langle \tilde{g}^2 \rangle$, it sufficiently shows a smaller softening.

Therefore, considering the adiabatic regime, competition, and coexistence between T_c and T_{CDW} for all doped levels, reveals that in the three hole-doped cases +0.1, +0.2 and +0.3, T_{CDW} is exceedingly greater than T_c and consequently, the CDW instability prevents access to the high-temperature superconductivity for mentioned doping levels.

C. Non-adiabatic effects

In metallic systems, ion dynamic affects the electron dynamics and leads to the excited state owing to the proximity of phonon energies and electron excited states [32]. Experimental realization of such dynamics on the phonon energies is observable in the form of the Raman frequency shift at the zone center so-called non-adiabatic effects [34, 35, 52, 53]. To explore this, a time-dependent perturbation theory (TDPT) is necessary for a full *ab initio* treatment of non-adiabatic effects. Since a full TDPT is complicated enough in practical terms of complexity of the accurate calculations, here, by pursuing Ref. [32], we adopt the following procedure to properly include the non-adiabatic effects. At the first necessary step for a specific \mathbf{q} vector, adiabatic self-consistent force constants, $C_{sr}(\mathbf{q}, 0, T_1)$, are calculated. Here T_1 is the electronic temperature applied in self-consistent calculations (T_1 is large enough to prevent Kohn anomaly). The non-adiabatic phonons can be naturally obtained by diagonalizing the phonon dynamical matrix related to non-adiabatic non-self-consistent force constants, $\tilde{C}(\mathbf{q}, \omega, T_0)$, at the physical temperature T_0 given by [32]:

$$\tilde{C}_{sr}(\mathbf{q}, \omega, T_0) = \Pi_{sr}(\mathbf{q}, \omega, T_0) + C_{sr}(\mathbf{q}, 0, T_1). \quad (11)$$

where Π_{sr} comprises both addition (subtraction) of the non-adiabatic (adiabatic) effects at the specific temperature T_0 (T_1) used in the related Fermi-Dirac distribution

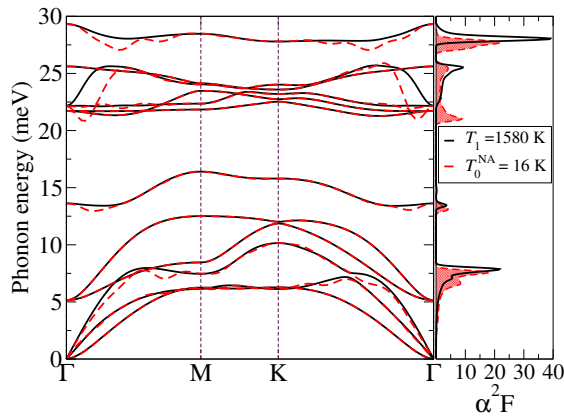


FIG. 7: (Color online) The phonon dispersion corresponding to adiabatic high ($T=1680$ K) and non-adiabatic low ($T=16$ K) electronic temperatures for a doping $+0.01$. The corresponding Eliashberg function is depicted at the right side of the plot. Also, fading out of CDW phase via non-adiabatic phonons at low temperatures is visible.

function $f_{\mathbf{k}m}$, respectively:

$$\begin{aligned} \Pi_{sr}(\mathbf{q}, \omega, T_0) = & \frac{2}{N_{\mathbf{k}}(T_0)} \sum_{\mathbf{k}, m, n}^{N_{\mathbf{k}}(T_0)} \frac{f_{\mathbf{k}m}(T_0) - f_{\mathbf{k}+\mathbf{q}n}(T_0)}{\varepsilon_{\mathbf{k}m} - \varepsilon_{\mathbf{k}+\mathbf{q}n} + \omega + i\eta} \times \\ & \mathbf{d}_{mn}^s(\mathbf{k}, \mathbf{k} + \mathbf{q}) \mathbf{d}_{nm}^r(\mathbf{k} + \mathbf{q}, \mathbf{k}) \\ & - \frac{2}{N_{\mathbf{k}}(T_1)} \sum_{\mathbf{k}, m, n}^{N_{\mathbf{k}}(T_1)} \frac{f_{\mathbf{k}m}(T_1) - f_{\mathbf{k}+\mathbf{q}n}(T_1)}{\varepsilon_{\mathbf{k}m} - \varepsilon_{\mathbf{k}+\mathbf{q}n}} \times \\ & \mathbf{d}_{mn}^s(\mathbf{k}, \mathbf{k} + \mathbf{q}) \mathbf{d}_{nm}^r(\mathbf{k} + \mathbf{q}, \mathbf{k}) \end{aligned} \quad (12)$$

where $N_{\mathbf{k}}(T_0)$ is \mathbf{k} -point grid at smearing T_0 and much larger than $N_{\mathbf{k}}(T_1)$ and we properly consider η as a positive real infinitesimal parameter. Furthermore, \mathbf{d}_{mn}^s are deformation potential matrix elements which properly include the derivative of the Kohn-Sham self-consistent potential with respect to the Fourier transform of the phonon displacements [32].

In the intra-sheet scattering process, when $|\varepsilon_{\mathbf{k}+\mathbf{q}} - \varepsilon_{\mathbf{k}}| \approx \omega$, the fundamental difference of the non-adiabatic and adiabatic frequencies, $\Delta\omega$ approximately specifies by $\Delta\omega \simeq N(\varepsilon_F)\langle\tilde{\mathbf{g}}^2\rangle$ at the Fermi surface [33–35]. Hence, this proper deference is remarkable for the doping cases $+0.01, +0.04, +0.1, +0.2$ and $+0.3$ encompassing large amounts for both the $N(\varepsilon_F)$ and $\langle\tilde{\mathbf{g}}^2\rangle$; essentially restating the considerable importance of the non-adiabatic effects for these hole-doped cases.

Having mentioned earlier, to obtain phonon energies within an adiabatic regime a coarse $24 \times 24 \times 1$ \mathbf{k} -point mesh and $T_1 = 1580$ K as a proper starting point are considered. While a dense enough \mathbf{k} -point grid $72 \times 72 \times 1$ is adopted for the calculation of non-adiabatic and adiabatic force constant matrices at more reduced temperatures. As depicted in Fig. 5 for the doping level $+0.1$, the amplitude of the Kohn anomaly decreases in the presence

of non-adiabatic effects. It is equally sought for the same electronic broadening $T_0 = 420$, and 470 K for the adiabatic one. In addition, the non-adiabatic calculations related to the electronic smearing $T_0^{NA} = 30$ (60) K (not shown here) express that the system is dynamically unstable at such temperature, which is lower (upper) than related superconducting temperature (44 K) given in Table. I.

Furthermore, the same calculations are repeated for doping $+0.2$ and $+0.3$. The results show that the system is still dynamically unstable close to the related superconducting transition temperature, 21 and 9 K, respectively. As a result, non-adiabatic effects shift only the CDW region to lower temperatures for elevated doped levels (i.e. $+0.1, +0.2$ and $+0.3$) and are not capable to suppress the formation of the CDW instability in these three cases. Therefore, it appears that the superconducting transition for three mentioned hole doping is unlikely to be accessible as a CDW phase forms before a superconductive phase.

In Fig. 7 high temperature phonon dispersion, $T_1 = 1580$ K, and non-adiabatic low temperature one with $T_0^{NA} = 16$ K are plotted along with their corresponding $\alpha^2\mathbf{F}$ for hole doping level 0.01. The system is stable even for temperatures considerably smaller than its $T_c = 65$ K (see equally Table. I). Notice that the $\alpha^2\mathbf{F}$ calculated based on non-adiabatic phonons gives marginally different $T_c=67$ K owing to the small softening at certain \mathbf{q} points. Accordingly, the low doped monolayer InSe likely shows a superconductive phase with maximum $T_c = 67$ K.

Notice that the convergence of Eq. (12) for η is carefully checked to adequately explain that this equation becomes practically η -independent when η decreases even as small as 0.0015 Ry. In addition, the desired results show that in the presence of the non-adiabatic effects, monolayer InSe is dynamically stable for all aforesaid doped levels at room temperature.

IV. CONCLUSION

In summary, based on the first-principle DFT and DFPT methods, the superconducting properties of pristine monolayer InSe employing the Migdal-Eliashberg theory are explored. We have also calculated the renormalized phonon dispersion owing to the electron-phonon coupling in both the adiabatic and non-adiabatic regimes for various temperatures and doping levels. We have further investigated the competition between CDW formation and the superconductive phase for the various hole and electron doping levels.

We have adequately discussed the most important phonon wave vectors leading to the remarkable electron-phonon coupling strength. That correctly expresses the significance of both bare susceptibility and nesting function below and beyond the Lifshitz transition point. Fur-

thermore, more analyses associated with polarization of the softened phonon mode at \mathbf{q}_{CDW} adequately explain that instability at this point mainly involves the in-plane displacements of the In atoms and the out of plane displacements of the Se atoms at the same time.

Our desired results show that in some hole-doped cases associated with elevated doping levels beyond the Lifshitz transition point (+0.1, +0.2, and +0.3 e/f.u.), T_{CDW} is much greater than T_c and consequently, CDW instability prevents access to superconductive phase. Whereas, for other hole doping levels, i.e. doping levels below Lifshitz transition point (+0.01 and +0.04 e/f.u.) and very deep hole doping level +0.4 e/f.u., T_{CDW} is lower than T_c and a maximum $T_c = 67$ K was achieved for hole doping level

+0.01 e/f.u. In the case of very deep hole doping +0.4 and electron doping rather small $T_c = 4$ and $T_c = 2$ K, respectively, are obtained. The non-adiabatic phonon effects correctly determine monolayer InSe becomes dynamically stable for different carrier concentrations at room temperature.

Acknowledgments

This work is supported by the Iran Science Elites Federation.

-
- [1] K. S. Novoselov, A. K. Geim, S. V. Morozov, D. Jiang, Y. Zhang, S. V. Dubonos, I. V. Grigorieva, and A. A. Firsov, "Electric field effect in atomically thin carbon films," *Science* **306**, 666 (2004).
- [2] K. K. Kim, A. Hsu, X. Jia, S. M. Kim, Y. Shi, M. Hofmann, D. Nezich, J. F. Rodriguez-Nieva, M. Dresselhaus, T. Palacios, and J. Kong, "Synthesis of monolayer hexagonal boron nitride on cu foil using chemical vapor deposition," *Nano Letters* **12**, 161 (2012).
- [3] M. Chhowalla, H. S. Shin, G. Eda, L.-J. Li, K. P. Loh, and H. Zhang, "The chemistry of two-dimensional layered transition metal dichalcogenide nanosheets," *Nature chemistry* **5**, 263 (2013).
- [4] B. Huang, G. Clark, E. Navarro-Moratalla, D. R. Klein, R. Cheng, K. L. Seyler, D. Zhong, E. Schmidgall, M. A. McGuire, D. H. Cobden, *et al.*, "Layer-dependent ferromagnetism in a van der Waals crystal down to the monolayer limit," *Nature* **546**, 270 (2017).
- [5] L. Li, Y. Yu, G. J. Ye, Q. Ge, X. Ou, H. Wu, D. Feng, X. H. Chen, and Y. Zhang, "Black phosphorus field-effect transistors," *Nature nanotechnology* **9**, 372 (2014).
- [6] P. Vogt, P. De Padova, C. Quaresima, J. Avila, E. Frantzeskakis, M. C. Asensio, A. Resta, B. Ealet, and G. Le Lay, "Silicene: Compelling experimental evidence for graphenelike two-dimensional silicon," *Phys. Rev. Lett.* **108**, 155501 (2012).
- [7] V. Zólyomi, N. D. Drummond, and V. I. Fal'ko, "Band structure and optical transitions in atomic layers of hexagonal gallium chalcogenides," *Phys. Rev. B* **87**, 195403 (2013).
- [8] V. Zólyomi, N. D. Drummond, and V. I. Fal'ko, "Electrons and phonons in single layers of hexagonal indium chalcogenides from ab initio calculations," *Phys. Rev. B* **89**, 205416 (2014).
- [9] G. Han, Z.-G. Chen, J. Drennan, and J. Zou, "Indium selenides: Structural characteristics, synthesis and their thermoelectric performances," *Small* **10**, 2747 (2014).
- [10] S. Lei, L. Ge, S. Najmaei, A. George, R. Kappera, J. Lou, M. Chhowalla, H. Yamaguchi, G. Gupta, R. Vajtai, A. D. Mohite, and P. M. Ajayan, "Evolution of the electronic band structure and efficient photo-detection in atomic layers of inSe," *ACS Nano* **8**, 1263 (2014), pMID: 24392873.
- [11] A. Politano, D. Campi, M. Cattelan, I. B. Amara, S. Jaziri, A. Mazzotti, A. Barinov, B. Gürbulak, S. Duman, S. Agnoli, *et al.*, "Indium selenide: an insight into electronic band structure and surface excitations," *Scientific reports* **7**, 3445 (2017).
- [12] B. Grbulak, M. ata, S. Dogan, S. Duman, A. Ashkhasi, and E. F. Keskenler, "Structural characterizations and optical properties of inSe and inSe:Ag semiconductors grown by bridgman/stockbarger technique," *Physica E: Low-dimensional Systems and Nanostructures* **64**, 106 (2014).
- [13] C. Julien and M. Balkanski, "Lithium reactivity with iiivi layered compounds," *Materials Science and Engineering: B* **100**, 263 (2003).
- [14] J. Chen, "Phonon-mediated superconductivity in electron-doped monolayer inSe: A first-principles investigation," *Journal of Physics and Chemistry of Solids* **125**, 23 (2019).
- [15] A. V. Lugovskoi, M. I. Katsnelson, and A. N. Rudenko, "Strong electron-phonon coupling and its influence on the transport and optical properties of hole-doped single-layer inSe," *Phys. Rev. Lett.* **123**, 176401 (2019).
- [16] G. W. Mudd, S. A. Svatek, T. Ren, A. Patan, O. Makarovskiy, L. Eaves, P. H. Beton, Z. D. Kovalyuk, G. V. Lashkarev, Z. R. Kudrynskiy, and A. I. Dmitriev, "Tuning the bandgap of exfoliated inSe nanosheets by quantum confinement," *Advanced Materials* **25**, 5714 (2013).
- [17] G. W. Mudd, A. Patan, Z. R. Kudrynskiy, M. W. Fay, O. Makarovskiy, L. Eaves, Z. D. Kovalyuk, V. Zlyomi, and V. Fal'ko, "Quantum confined acceptors and donors in inSe nanosheets," *Applied Physics Letters* **105**, 221909 (2014).
- [18] W. Feng, W. Zheng, X. Chen, G. Liu, and P. Hu, "Gate modulation of threshold voltage instability in multilayer inSe field effect transistors," *ACS Applied Materials & Interfaces* **7**, 26691 (2015), pMID: 26575205.
- [19] X. Cui, G.-H. Lee, Y. D. Kim, G. Arefe, P. Y. Huang, C.-H. Lee, D. A. Chenet, X. Zhang, L. Wang, F. Ye, *et al.*, "Multi-terminal transport measurements of mos 2 using a van der waals heterostructure device platform," *Nature nanotechnology* **10**, 534 (2015).
- [20] C. Sun, H. Xiang, B. Xu, Y. Xia, J. Yin, and Z. Liu, "Ab initio study of carrier mobility of few-layer InSe," *Applied Physics Express* **9**, 035203 (2016).

- [21] E. G. Marin, D. Marian, G. Iannaccone, and G. Fiori, “First-principles simulations of fets based on two-dimensional inse,” *IEEE Electron Device Letters* **39**, 626 (2018).
- [22] J. Bardeen, L. N. Cooper, and J. R. Schrieffer, “Theory of superconductivity,” *Phys. Rev.* **108**, 1175 (1957).
- [23] T. Cao, Z. Li, and S. G. Louie, “Tunable magnetism and half-metallicity in hole-doped monolayer gase,” *Phys. Rev. Lett.* **114**, 236602 (2015).
- [24] M. Dresselhaus, G. Chen, M. Tang, R. Yang, H. Lee, D. Wang, Z. Ren, J.-P. Fleurial, and P. Gogna, “New directions for low-dimensional thermoelectric materials,” *Advanced Materials* **19**, 1043 (2007).
- [25] N. T. Hung, A. R. T. Nugraha, and R. Saito, “Two-dimensional inse as a potential thermoelectric material,” *Applied Physics Letters* **111**, 092107 (2017).
- [26] S. Wu, X. Dai, H. Yu, H. Fan, J. Hu, and W. Yao, “Magnetisms in p -type monolayer gallium chalcogenides (gase, gas),” arXiv preprint arXiv:1409.4733 (2014).
- [27] B. M. Ludbrook, G. Levy, P. Nigge, M. Zonno, M. Schneider, D. J. Dvorak, C. N. Veenstra, S. Zhdanovich, D. Wong, P. Dosanjh, C. Straßer, A. Stöhr, S. Forti, C. R. Ast, U. Starke, and A. Damascelli, “Evidence for superconductivity in li-decorated monolayer graphene,” *Proceedings of the National Academy of Sciences* **112**, 11795 (2015).
- [28] S. Ichinokura, K. Sugawara, A. Takayama, T. Takahashi, and S. Hasegawa, “Superconducting calcium-intercalated bilayer graphene,” *ACS Nano* **10**, 2761 (2016).
- [29] G. Profeta, M. Calandra, and F. Mauri, “Phonon-mediated superconductivity in graphene by lithium deposition,” *Nature physics* **8**, 131 (2012).
- [30] M. Xue, G. Chen, H. Yang, Y. Zhu, D. Wang, J. He, and T. Cao, “Superconductivity in potassium-doped few-layer graphene,” *Journal of the American Chemical Society* **134**, 6536 (2012).
- [31] S. Baroni, S. de Gironcoli, A. Dal Corso, and P. Giannozzi, “Phonons and related crystal properties from density-functional perturbation theory,” *Rev. Mod. Phys.* **73**, 515 (2001).
- [32] M. Calandra, G. Profeta, and F. Mauri, “Adiabatic and nonadiabatic phonon dispersion in a wannier function approach,” *Phys. Rev. B* **82**, 165111 (2010).
- [33] M. Lazzeri and F. Mauri, “Nonadiabatic kohn anomaly in a doped graphene monolayer,” *Phys. Rev. Lett.* **97**, 266407 (2006).
- [34] A. M. Saitta, M. Lazzeri, M. Calandra, and F. Mauri, “Giant nonadiabatic effects in layer metals: Raman spectra of intercalated graphite explained,” *Phys. Rev. Lett.* **100**, 226401 (2008).
- [35] D. Novko, Q. Zhang, and P. Kaghazchi, “Nonadiabatic effects in raman spectra of alcl_4 -graphite based batteries,” *Phys. Rev. Applied* **12**, 024016 (2019).
- [36] P. Giannozzi, S. Baroni, N. Bonini, M. Calandra, R. Car, C. Cavazzoni, D. Ceresoli, G. L. Chiarotti, M. Cococcioni, I. Dabo, A. D. Corso, S. de Gironcoli, S. Fabris, G. Fratesi, R. Gebauer, U. Gerstmann, C. Gougoussis, A. Kokalj, M. Lazzeri, L. Martin-Samos, N. Marzari, F. Mauri, R. Mazzarello, S. Paolini, A. Pasquarello, L. Paulatto, C. Sbraccia, S. Scandolo, G. Sclauzero, A. P. Seitsonen, A. Smogunov, P. Umari, and R. M. Wentzcovitch, “Quantum espresso: a modular and open-source software project for quantum simulations of materials,” *Journal of Physics: Condensed Matter* **21**, 395502 (2009).
- [37] M. Wierzbowska, S. de Gironcoli, and P. Giannozzi, “Origins of low-and high-pressure discontinuities of $t_{-}\{c\}$ in niobium,” arXiv preprint cond-mat/0504077 (2005).
- [38] N. Marzari and D. Vanderbilt, “Maximally localized generalized wannier functions for composite energy bands,” *Phys. Rev. B* **56**, 12847 (1997).
- [39] I. Souza, N. Marzari, and D. Vanderbilt, “Maximally localized wannier functions for entangled energy bands,” *Phys. Rev. B* **65**, 035109 (2001).
- [40] A. A. Mostofi, J. R. Yates, Y.-S. Lee, I. Souza, D. Vanderbilt, and N. Marzari, “wannier90: A tool for obtaining maximally-localised wannier functions,” *Computer Physics Communications* **178**, 685 (2008).
- [41] S. Ponc, E. Margine, C. Verdi, and F. Giustino, “Epw: Electronphonon coupling, transport and superconducting properties using maximally localized wannier functions,” *Computer Physics Communications* **209**, 116 (2016).
- [42] M. Verstraete and X. Gonze, “Smearing scheme for finite-temperature electronic-structure calculations,” *Phys. Rev. B* **65**, 035111 (2001).
- [43] O. R. Albertini, A. Y. Liu, and M. Calandra, “Effect of electron doping on lattice instabilities in single-layer $1h - \text{tas}_2$,” *Phys. Rev. B* **95**, 235121 (2017).
- [44] W. Kohn, “Image of the fermi surface in the vibration spectrum of a metal,” *Phys. Rev. Lett.* **2**, 393 (1959).
- [45] A. Migdal, “Interaction between electrons and lattice vibrations in a normal metal,” *Sov. Phys. JETP* **7**, 996 (1958).
- [46] G. Eliashberg, “Interactions between electrons and lattice vibrations in a superconductor,” *Sov. Phys. JETP* **11**, 696 (1960).
- [47] P. B. Allen and R. Dynes, “Transition temperature of strong-coupled superconductors reanalyzed,” *Physical Review B* **12**, 905 (1975).
- [48] Deformation potential is defined as $d_{nk, m\mathbf{k}+\mathbf{q}}^{r,s} = \langle \psi_{m, \mathbf{k}+\mathbf{q}} | \frac{\partial V_{\mathbf{k}, \mathbf{s}}}{\partial u_{\mathbf{q}}} | \psi_{n, \mathbf{k}} \rangle$.
- [49] D. K. Efetov and P. Kim, “Controlling electron-phonon interactions in graphene at ultrahigh carrier densities,” *Phys. Rev. Lett.* **105**, 256805 (2010).
- [50] D. N. Esfahani and R. Asgari, “Superconducting critical temperature of hole doped blue phosphorene,” arXiv preprint arXiv:1710.05554 (2017).
- [51] A. V. Lugovskoi, M. I. Katsnelson, and A. N. Rudenko, “Electron-phonon properties, structural stability, and superconductivity of doped antimonene,” *Phys. Rev. B* **99**, 064513 (2019).
- [52] D. Novko, “Broken adiabaticity induced by lifshitz transition in mos 2 and ws 2 single layers,” *Communications Physics* **3**, 1 (2020).
- [53] F. Giustino, “Electron-phonon interactions from first principles,” *Rev. Mod. Phys.* **89**, 015003 (2017).